Tech Science Press

Shear Flows in the Near-Turbulent Wake Region of High Speed Trains

Liang Ce and Yongchen Pan[*]

China Academy of Railway Sciences Co., Ltd., Beijing, 100081, China
[*]Corresponding Author: Yongchen Pan. Email: l_cee@163.com.

Abstract: Two flow cases for scaled high speed train models with different length are numerically analyzed in the framework of the improved delayed detached-eddy simulation model. Specific attention is paid to the shear flows and related mechanisms in the near turbulent wake created by these moving models. In particular, a comparative analysis is made on the distributions of turbulent kinetic energy (TKE) and turbulence production (TP) in planes perpendicular to the streamwise direction. The numerical results suggest that, in the wake region very close to the tail, significant TKE and TP can be ascribed to the dynamic interaction between powerful eddies and strong shear, which explain why these quantities are sensitive to the shear strength. The shear flows are essentially governed by the boundary layers developing along the streamwise direction on the train surfaces, especially from the under-body region and the side walls. For other positions located in the downstream direction away from the tail, the interaction of vortices with the non-slip ground serves as a mechanism to promote transfer of energy from weak eddies to turbulence through the shear present in planes parallel to the ground.

Keywords: High speed train; near turbulent wake; shear flow; turbulent kinetic energy; turbulence production

1 Introduction

A high-speed train running may result in some aerodynamic issues, namely slipstream, drag, acoustics, and so on, which have drawn much interests of thousands of scholars and researchers [1–3].

Among the aerodynamic effects, there exists important vortex structure in the turbulent wake of a high-speed train. Bell et al. [4–6] pointed out that the twin counter-rotating streamwise vortices, which are similar to the flow structures discussed by Morel [7] and play important roles on the slipstream phenomenon, are remarkable features for the near wake of a high-speed train. The formation and shedding of the wake vortices happen around the tail, and make a significant contribution to the notable pressure drag [8]. It was reported that the impressive noise level comes from the tail of a high-speed train due to the flow coherent structures in the turbulent wake [9].

A high-speed train has the feature of large slenderness ratio (length/height ratio), so the boundary-layer thickness on the train surface will be much greater than that for other ground vehicles. In this way, any shear layers separated will also be much thicker because of the streamlined tail shape of trains [10–12]. Rowe et al.

[13] suggested that the displacement thickness represents the effective diffusion distance between the two shear layers at the trailing edge of a two-dimensional plate and the momentum thickness the intensity of vorticity within the inner part of the boundary layer, and the experimental results indicate that the base pressure and vortex shedding frequency will be evidently influenced by the shape factor (ratio of the displacement thickness to the momentum thickness), which is an important parameter. Then, from the numerical results of Muld et al. [14], it was manifested that the boundary-layer momentum thickness on the roof of a high-speed train satisfactorily fits the empirical expression for the momentum thickness of turbulent boundary layer on a plate. And the wake flow was reconstructed by the method called proper orthogonal decomposition, obtaining the characteristics of the vortex structures in the near wake and explaining the relation between the momentum thickness and the vortex shedding frequency.

Separated shear flows are important to the formation and shedding processes of the wake vortices. When the wake runs downwards, the dynamic interaction between the mean shear flow and the turbulent eddies is significantly important to the wake, and the eddies, as believed by Tennekes & Lumley [15], may have the capacity for extracting energy from the mean flow as a result of that the shear rotates and strains turbulent vortices. In this paper, from the viewpoint of turbulent energy, the shear flows in the near turbulent wake of high-speed trains was investigated through the discussion on turbulent kinetic energy and turbulence production to help in the further understanding on the wake-related issues.

2 Numerical Simulations

2.1 Simplified High Speed Train Model and Computational Domain

The train geometry in this paper is a 1/30th-scale model based on the CRH380A high speed train. Two different flow cases with different model lengths are simulated for comparative analysis in the discussions below. The first flow case (M2) contains a short train set consisting of two cars (namely a head and a trailing car), and the other flow case (M4) contains a long train which has a total of four cars, including two intermediate cars. The scaled models are simplified without several rough elements, namely pantographs, inter-car gaps. And generic bogies are not considered, and their cavities are sealed off by adding cover plates. Hence, the basic features of aerodynamic shapes (slender, small aspect ratio, and streamlined head and tail) are focused on the import vortex structure of the turbulent wake.

The Reynolds number (Re_∞) of the incoming flow reaches about 300,000 based on the free stream velocity $U_\infty = 40$ m/s, and the model height, $H \approx 0.12$ m. Correspondingly, the Mach number is about 0.12, which is smaller than 0.3, so that the air can be thought as incompressible fluid. The computational domains are shown in Fig. 1. In addition, the streamwise lengths of the two train models are about 15 H and 29 H, respectively.
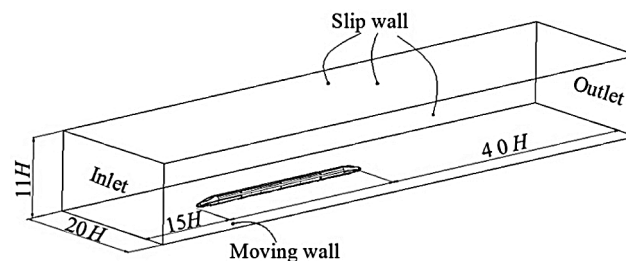

Figure 1: Computational domain and boundary conditions

2.2 Mathematical Model

In the present simulation cases for the incompressible fluid, the governing equation can be expressed as follows:

$$\frac{\partial u_i}{\partial t} + u_j \frac{\partial u_i}{\partial x_j} = \frac{1}{\rho}\frac{\partial}{\partial x_j}(-p\delta_{ij} + 2\mu s_{ij}) \tag{1}$$

$$\frac{\partial u_i}{\partial x_i} = 0 \tag{2}$$

where δ_{ij} denotes Kronecker symbol and μ dynamic viscosity, strain rate s_{ij} is defined as $s_{ij} = \frac{1}{2}(\frac{\partial u_i}{\partial x_j} + \frac{\partial u_j}{\partial x_i})$.

To gain accurate information on the large-scale flow structures around a bluff body, an approach called detached eddy simulation (DES) can perform well and has been verified to be a promising turbulent model for the investigation on the wake of a HST. (e.g., [16–18] for reference).

This hybrid method has advantages of lowering the demands on computer hardwares and improving the computational efficiency in comparison with the large eddy simulation (LES), because the same grid resolution as the Reynolds-averaged Navier-Stokes (RANS) model is available in the boundary layer. In this work, the improved delayed DES (IDDES), based on the SST k-ω turbulence model, is utilized, in which a hybrid length scale, l_{hyb}, is calculated to add Wall-Modeled LES (WMLES) capability used for the similar level of resolution typically required for the classic LES study on turbulent boundary layers.

$$l_{\mathrm{hyb}} = \widetilde{f_d}(1 + f_e)l_t + (1 - \widetilde{f_d})C_{\mathrm{DES}}\Delta_{\mathrm{IDDES}} \tag{3}$$

where l_t serves as the turbulent length scale, in the IDDES model, $\widetilde{f_d}$ is used to combine the WMLES and DDES branches, f_e is elevating function, and C_{DES} is a model constant.

$$\Delta_{\mathrm{IDDES}} = \min(\max(0.15d, 0.15\Delta_{\max}, \Delta_{\min}), \Delta_{\max}) \tag{4}$$

where d is the distance to the wall, $\Delta_{\min}$ is the smallest distance between the cell center under consideration and the cell centers of the neighboring cells, $\Delta_{\max}$ is the largest distance between the cell center under consideration and the cell centers of the neighboring cells.

More details for the turbulence model can be seen in such literatures as the reference [19].

The boundary conditions are also shown in Fig. 1. The velocity inlet condition was set with the magnitude and direction, namely the velocity (U_∞, 0, 0) across the whole inlet surface, and turbulent intensity (*TI*) are presented across the inlet and set as constants, *TI* = 0.05. The pressure outlet is adopted and set to zero gauge pressure, and the method, Boundary-Normal, specifies the flow direction for the outlet boundary. In terms of the wall surfaces of the computational domain, the ground is set as a moving wall boundary condition with the velocity (U_∞, 0, 0), and the train model surface as a stationary wall condition, owing to the relative motion between the ground and train. The two walls are no-slip which means that the fluid adjacent to the wall surfaces has to move with the same velocity as the walls. And this boundary condition is implemented in the solver with a hybrid wall treatment providing a more realistic modeling than either the low-Re or the high-Re treatments (especially for when the wall-cell centroid falls in the buffer region). In addition, the slip wall boundary condition is applied to the top and side walls of the computational domain.

2.3 Numerical Method

The Navier-Stokes (N-S) equations are discretized by the finite volume method, and the unsteady flow is numerically solved with the coupled implicit solver, and the pressure-velocity coupling use the Pressure Implicit with Splitting of Operator (PISO) algorithm [20]. The temporal discretization accuracy is of the second-order implicit scheme. And the second-order and bounded central-differencing discretization schemes are employed respectively for RANS and LES modes to evaluate face values for convection and diffusion fluxes. Besides, a second-order scheme is used in the turbulence model for turbulent quantities.

During most of iteration, the time step is 0.02 H/U_∞, and the CFL (Courant-Friedrichs-Lewy) number remains smaller than one, while the smaller time step size (Δt) and lower CFL for the implicit solver help to avoid divergence and benefit to improve accuracy in the numerical calculation initially. For the procedure of data sampling, it takes 200 H/U_∞ to obtain relevant time-averaged quantities.

2.4 Grids

The topology of the trim-hexa mesh is adopted for the present numerical simulation. Concretely speaking, there are 12 prism layers close to the wall surface of the model body (as seen in the Fig. 2a), and the dimensionless thickness of the first prism layer, δ^+, at the wall surface is approximately equal to the magnitude of $O(1)$. Away from the wall boundaries, the grids consist of the perfect hexa cells which are connected to the prism layers by the trimmed cells. In order to appropriately resolve the flow structures, five zones around the model body are refined with finer grids, of which three zones are placed in the wake flow, as shown in Fig. 2b.
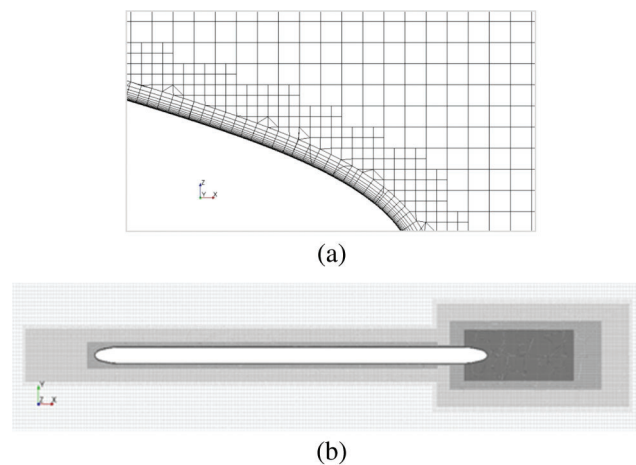

(a)

(b)

Figure 2: Schematic view of the topology near the train surface (a) and the zones with grids refined (b)

In order to prove the calculated results satisfying grid independence, three different numerical grids have been generated and tested by simulating the flow field around a model of the train with three cars. The fine mesh (FM), medium mesh (MM) and coarse mesh (CM) consist of 17.9, 10.5 and 6.3 million cells, respectively.

Time-averaged profiles of streamwise velocity U, and turbulent kinetic energy (TKE), $K=\frac{1}{2}(\overline{u'u'} + \overline{v'v'} + \overline{w'w'})$, (where u', v' and w' denote the velocity fluctuation components in the streamwise (x), spanwise (y) and normal (z) directions.) in the near wake of the train shown in Fig. 3. It is shown that the trend of the MM curves can stay in step with the FM curves very well, and there is only some small difference between them. However, the CM curves of velocity in Fig. 3b deviates clearly from the two other curves, and the CM also shows inconsistence in TKE. Therefore, the CM is thought to be unacceptable, but the MM is considered to be adequate.

For the M2 and M4 cases, the cell sizes in the refined zones are controlled within the range from 0.02 H to 0.08 H in the present numerical investigation, and the computational domains contain over 9.3 and 12.1 million cells, respectively.
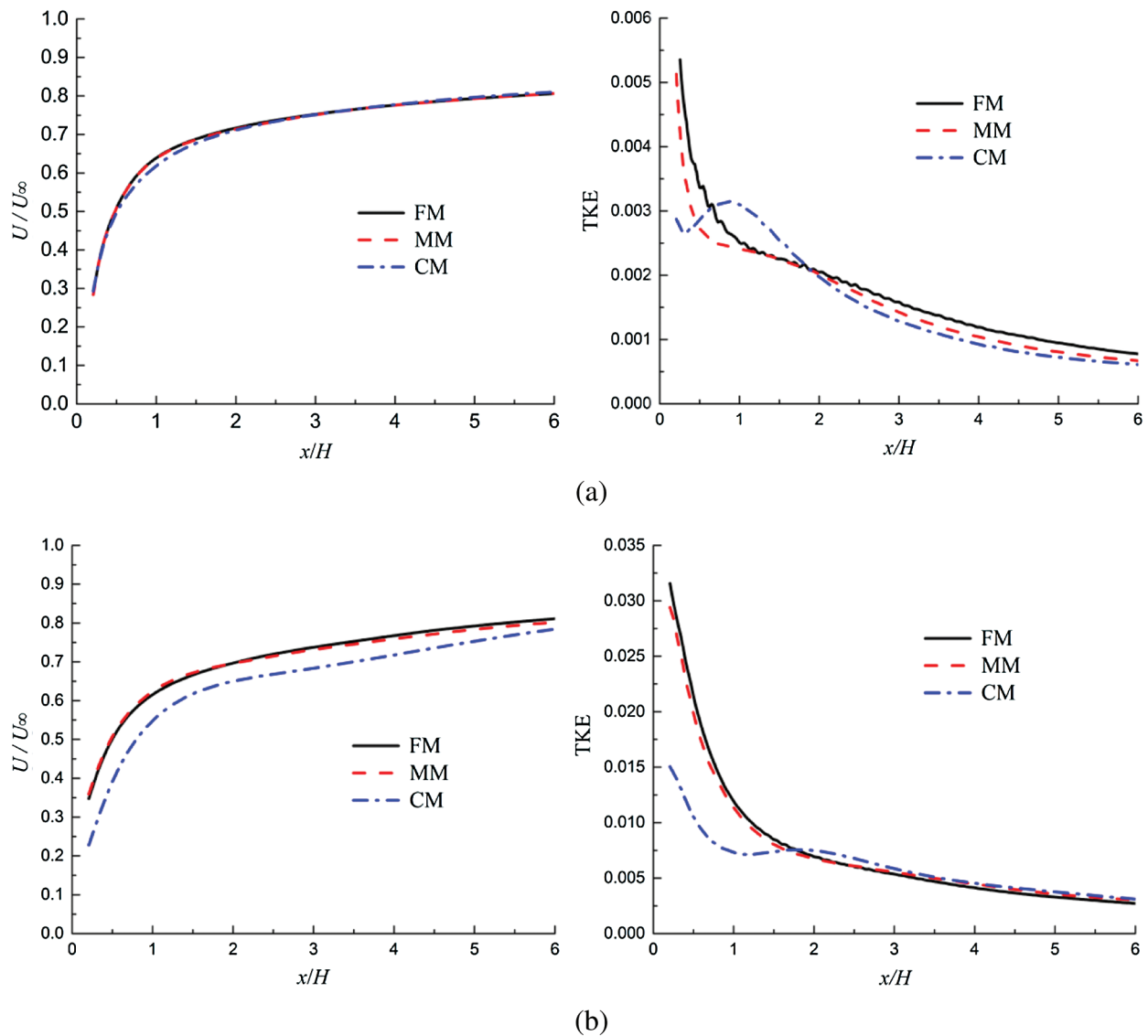
Figure 3: Time-averaged profiles of streamwise velocity and TKE as a function of the streamwise distance away from the tail in the near wakes of the trains with the three different grids. (a) $y = 0$ and (b) $y = 0.25H$

3 Numerical Results and Discussions

3.1 Validation

Slipstream is regarded as an important characteristic of the wake flow of a HST and closely related to the wake structure. Considering that the train model is stationary, the slipstream velocity, us, is herein defined as the horizontal velocity:

$$u_S = \sqrt{(U_\infty - u)^2 + v^2} \qquad (5)$$

where u and v denote the transient velocities in the streamwise (x) and spanwise (y) directions, respectively.

Fig. 4 gives the slipstream velocity curves from the present simulation and the experimental investigation. In the wind-tunnel experiments by Bell et al. [21], the closed test section is fitted with a

splitter plane to weaken ground boundary layer effects. Similarly, the effects can be distinctively reduced due to the non-slip moving ground in the numerical simulation. More information on the experiment will be seen in the reference paper.
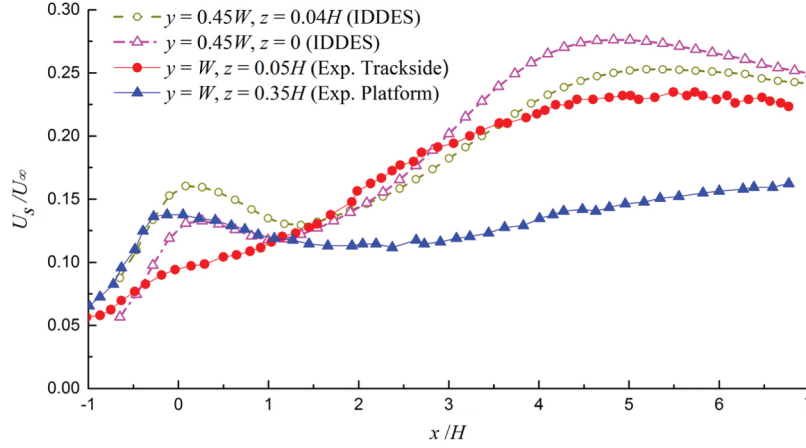

Figure 4: Time-averaged slipstream as a function of the streamwise distance from the tail

Obviously, the numerical curves exhibit common features of slipstream profile, namely, the local peaks at the tail and the maxima at downstream x-positions in the near wake. And by comparison, it can be observed that the numerical curves agree well with the experimental curve for the trackside case, while the mild curve with its peak postponed may be due to that the air flow is restricted by the platform structure. Anyway, it can be believed that the present simulation is able to gain convincing information on the near turbulent wake.

W denotes the width of the train modeled. If not stated, $x = 0$ corresponds to the end of tail, and $y = 0$ the middle in the spanwise direction for the model and surround flow; $z = 0$ corresponds to the model bottom for the present simulation, and to the top of rail for the experiments.

3.2 Turbulent Kinetic Energy

Fig. 5 displays wake vortex structure identified by the Q criterion. The second invariant, Q, of is defined as

$$Q = \tfrac{1}{2}\left(||\Omega||^2 - ||S||^2\right) \tag{6}$$

where $||S|| = [\mathrm{tr}(SS^{\mathrm{t}})]^{1/2}$ and $||\Omega|| = [\mathrm{tr}(\Omega\Omega^{\mathrm{t}})]^{1/2}$, and S and Ω are the symmetric and antisymmetric components of ∇u [22].

It can be observed in Fig. 5 that the wake vortex structure in the M2 case seem similar with that in the M4 case, namely, the twin turbulent vortices appear on the two flanks of the tail, and when propagating downstream, streamwise vortex streets take shape through the turbulent wake. However, a major difference between the two flow cases is that the length scales of the wake vortices seem larger for the M4 case than for the M2 case, for more fully-developed boundary layer layers lead to thicker shear layers with relative low vortex strength (low vorticity).

In Fig. 5, the colors dyeing the Q-isosurface present the variation of TKE, and the blue and red colors stand for the low and high values, respectively. As shown in Fig. 5, a great amount of turbulent energy is contained by the turbulent eddies near the tail that play the significant roles during formation and shedding of streamwise vortices.
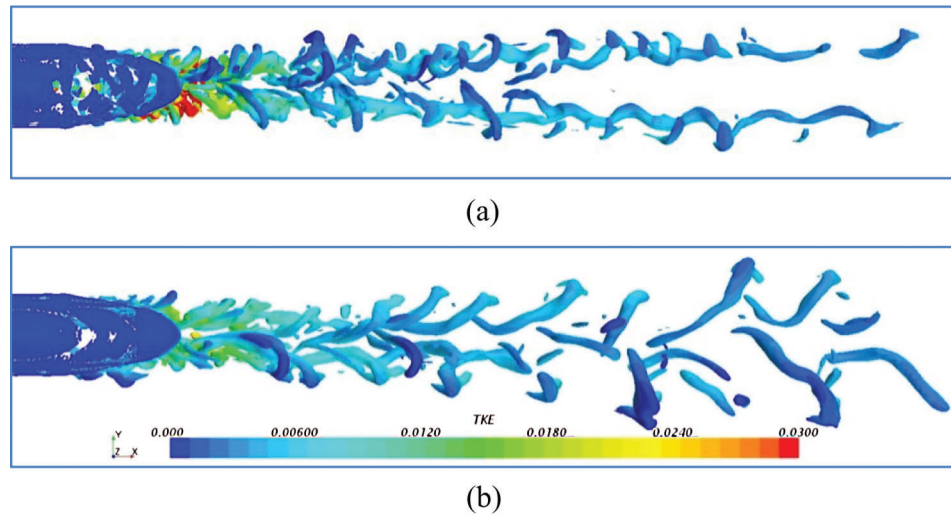
(a)

(b)

Figure 5: Wake vortex structure identified by the Q-criterion ($Q = 50000$ s^{-2}). (a) M2 and (b) M4

Fig. 6 shows the variations of the K distributions in the local y-z plane for each of three streamwise positions, $x = 0$, H and $2H$. (According to the position of the train model in the computational domain, the tail tip of the trailing car corresponds to $x = 0$ (streamwise) and $y = 0$ (spanwise), and the model bottom $z = 0$ (normal). In addition, unless there are additional specifications given, the free stream velocity, U_∞, serves as the characteristic velocity, and the model height, H, as the characteristic length scale, and the two quantities will be used for dimensionless variables scaling in the discussion below.)

In Fig. 6, the symmetry about the axis $y = 0$ and the change along the streamwise direction are clearly presented for the K distributions in the y-z plane. On one hand, in the local y-z plane at $x = 0$, the impressive peak approximately at $y = 0$ is displayed especially for the M2 case, and the results indicate that the high-value energy is mainly gathered at the lower altitude around the model bottom ($z = 0$). On the other hand, at $x = H$ and $2H$, the TKE falls obviously, and the symmetrical distribution with a couple of mild peaks is shown in Figs. 6b and 6c.

In general, the energy distributions for the two flow cases seem similar to each other at each of the three streamwise positions. Differently, the K distributions in Fig. 6a suggest that the turbulent eddies for the M4 case contain much less energy than for the M2 case. However, except for the distributional extent of the TKE probably related to the different eddy length scales, as shown in Figs. 6b and 6c, the nearly same magnitude of energy in the near wake away from the tail can be observed for both the M2 case and the M4 case.

3.3 Turbulence Production

Turbulent eddies need shear to maintain their energy, and those powerful eddies are rotated and strained by the mean shear to maintain the good correlations both between the streamwise and spanwise velocity fluctuations and between the streamwise and normal velocity fluctuations, resulting in efficient energy transfer. In the equation of turbulent energy budget, the turbulence production (TP) can be expressed as

$$P_{xy} = -\overline{u'v'}S_{xy} - \overline{v'u'}S_{yx} \text{ and } P_{xz} = -\overline{u'w'}S_{xz} - \overline{w'u'}S_{zx} \qquad (7)$$

The mean flow is along the x-direction, and that $\frac{\partial}{\partial x} \ll \frac{\partial}{\partial y}$ and $\frac{\partial}{\partial x} \ll \frac{\partial}{\partial z}$ can be equally acceptable here, hence Eq. (4) may be written as
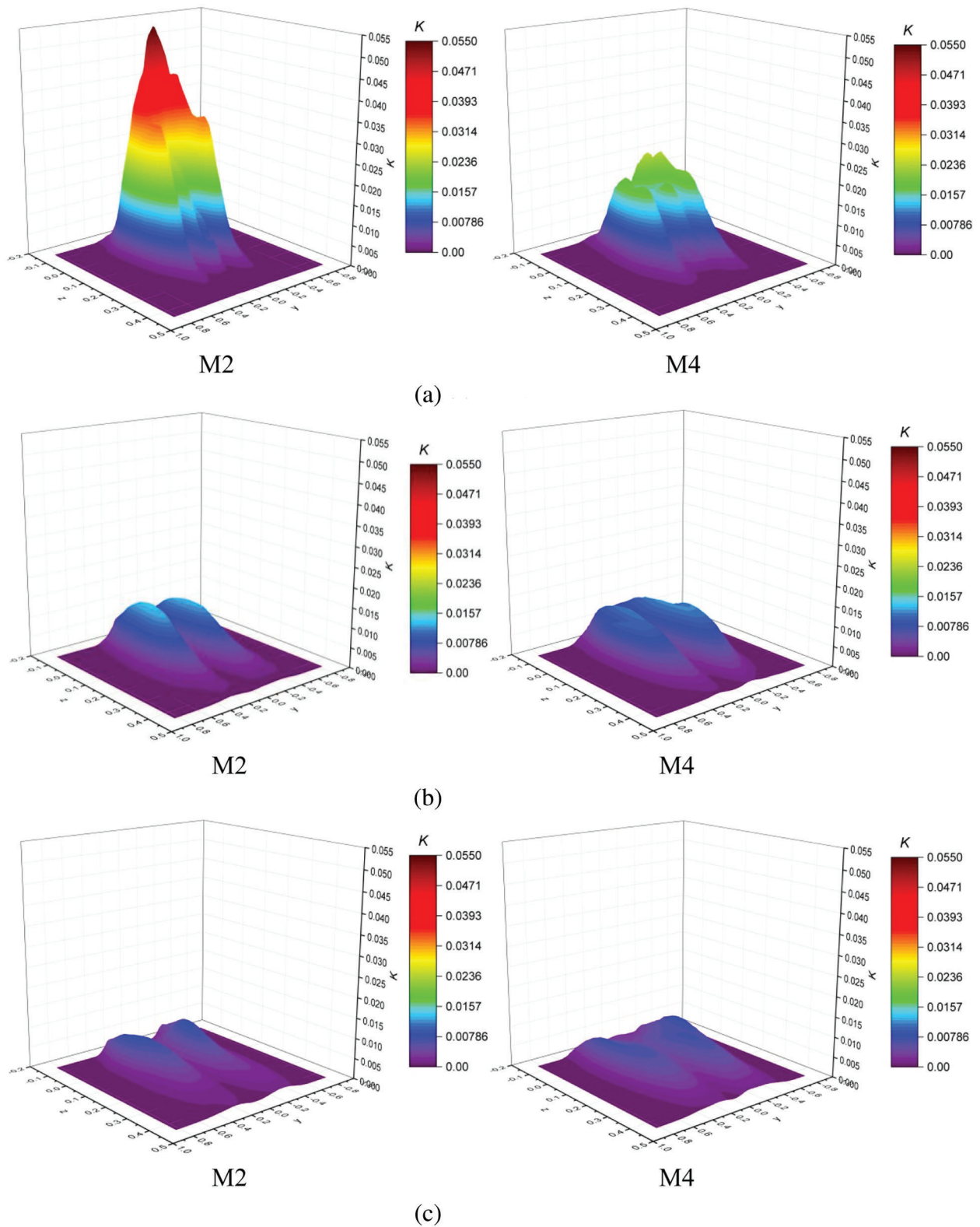
Figure 6: Variations of the K distribution as a function of the spanwise (y) and normal (z) coordinates at the three streamwise positions ($x = 0$, H and $2H$). (a) $x = 0$ (b) $x = H$ and (c) $x = 2H$

$$P_{xy} = -\overline{u'v'}\frac{\partial U}{\partial y} \text{ and } P_{xz} = -\overline{u'w'}\frac{\partial U}{\partial z} \tag{8}$$

The separated shear flows are dependently from the boundary layers developed along the streamwise direction on the roof, sides and underbody of the train modelled, and Eq. (5) indicates that the mean shear strain rates, namely the spanwise (y) and normal (z) gradients of the mean streamwise velocity, U, can have the significant influences on the turbulent vortices and TP.

The P_{xz} and P_{xy} distributions in the y-z plane at $x = 0$, H and $2H$ are shown in Figs. 7 and 8, respectively.
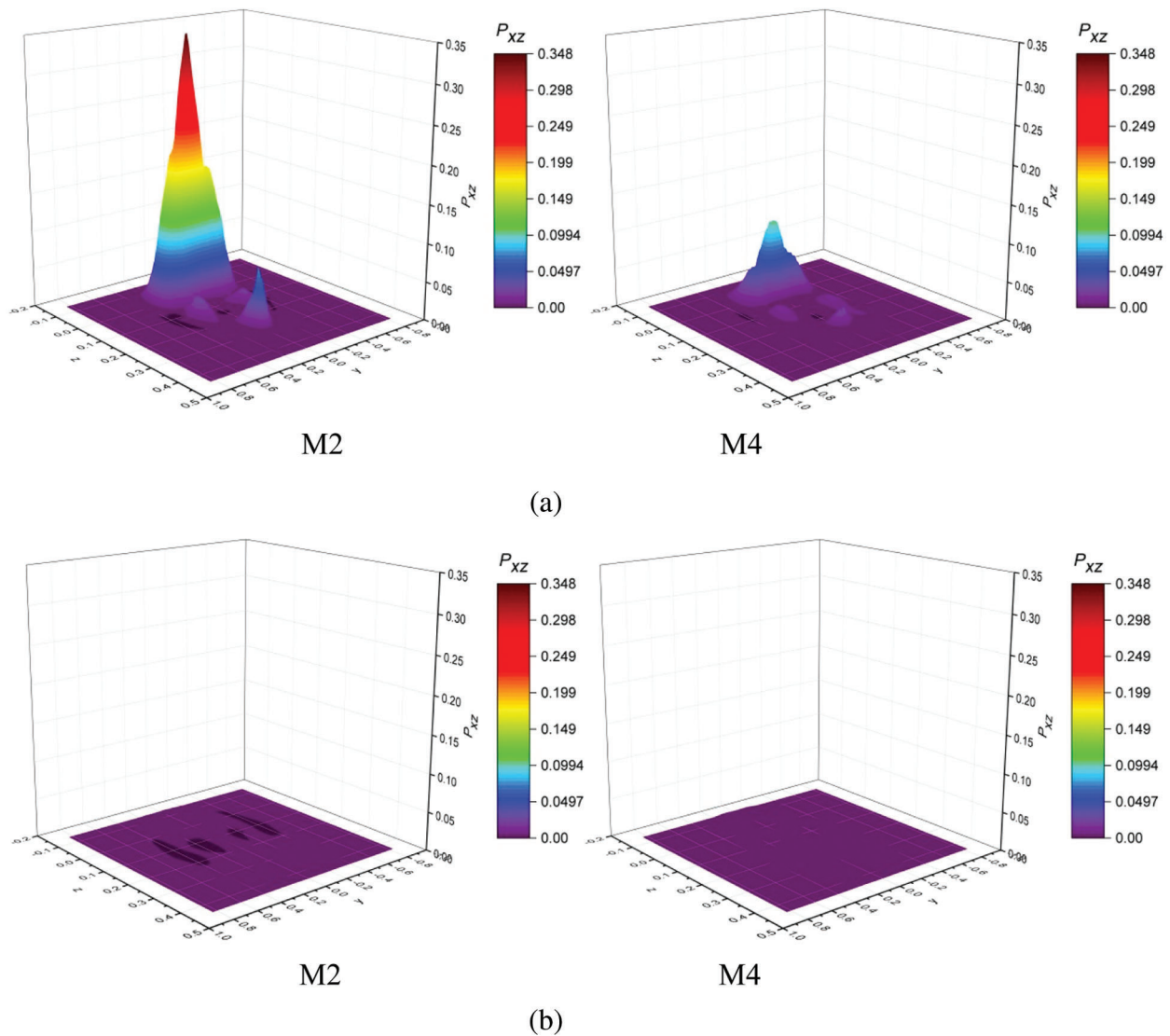

Figure 7: Variations of the P_{xz} distribution as a function of the spanwise (y) and normal (z) coordinates at the different streamwise positions ($x = 0$, H and $2H$). (a) $x = 0$ and (b) $x = H$

Figure 8: Variations of the P_{xy} distribution as a function of the spanwise (y) and normal (z) coordinates at the different streamwise positions ($x = 0$, H and $2H$). (a) $x = 0$ (b) $x = H$ and (c) $x = 2H$
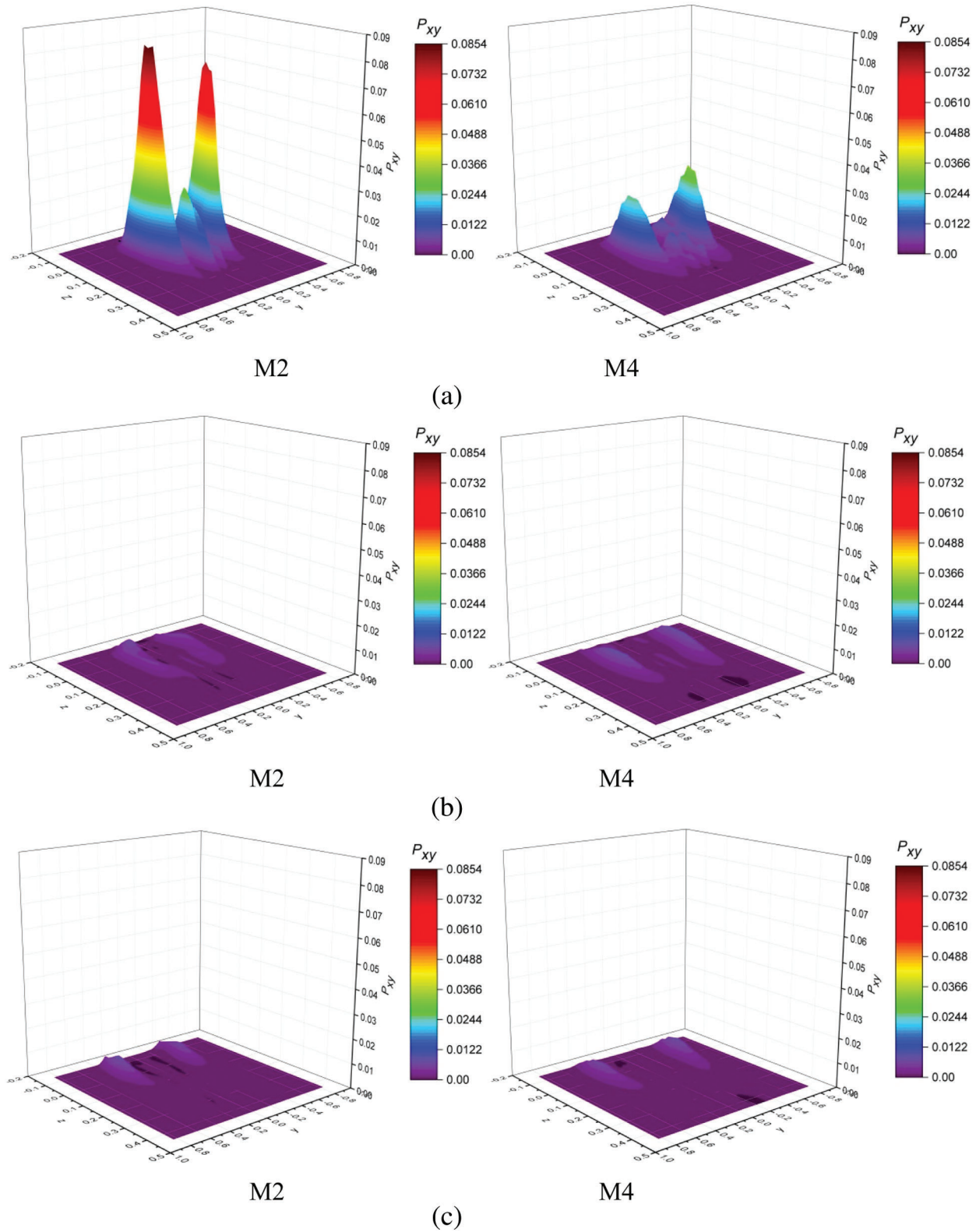
For the streamwise position $x = 0$, as shown in Fig. 7a, the P_{xz} distributions have the same features with the K distributions in Fig. 6a, namely the remarkable peak at $y = 0$ and the spanwise symmetry, and the turbulent energy produced is mostly situated at the lower altitude about the model bottom ($z = 0$); but the negligible peak at the higher altitude seems to be related to the shear flow separated from the roof. In Fig. 7b, at $x = H$, the P_{xz} magnitudes are cut down by a large margin and the peaks drop by two orders of magnitude, so these notable changes indicate that the eddies lose the ability to rely on the mean shear, $\frac{\partial U}{\partial z}$, for the TP. Besides, comparing the M2 case with the M4 case, the effect of the varied model lengths on the TP can be prominently reflected by the P_{xz} distributions at $x = 0$ for the M2 and M4 cases in Fig. 7a. But the substantive differentials fail to be brought on between the P_{xz} distributions at the downstream position $x = H$ in Fig. 7b, in other words, the varied streamwise lengths play few roles in the TP away from the tail.

The P_{xy} distributions are in sharp contrasts to the P_{xz} distributions. Fig. 8a shows the P_{xy} distributions at $x = 0$ with a couple of peaks are symmetrical in the spanwise direction, resembling the K distributions at $x = H$ and $2H$ in Figs. 6b and 6c, however, the peak values are much smaller than the P_{xz} maximum in Fig. 7a. Figs. 8b and 8c indicate that the distributional form almost remains unchanged downstream along the streamwise direction, but the rate of production of turbulent energy has to decline distinctly. Nonetheless, it can be suggested in Fig. 9 that, due to the mean shear in the x-y plane, turbulent eddies can maintain their capacity for extracting energy from the mean flow more efficiently in comparison with the P_{xz} distribution at $x = 2H$. In addition, comparatively speaking, the effect of the model lengths on the TP is saliently reflected by the P_{xy} distributions at $x = 0$ for the M2 and the M4 case in Fig. 8a, namely the P_{xy} peaks for the M4 case are evidently smaller than those for the M2 case. But the length effect cannot play any roles in these distributions at the downstream positions ($x = H$ and $2H$) away from the tail, as shown in Figs. 8b and 8c, the different lengths fail to cause dissimilarity between the P_{xy} distributions for the M2 and the M4 case.
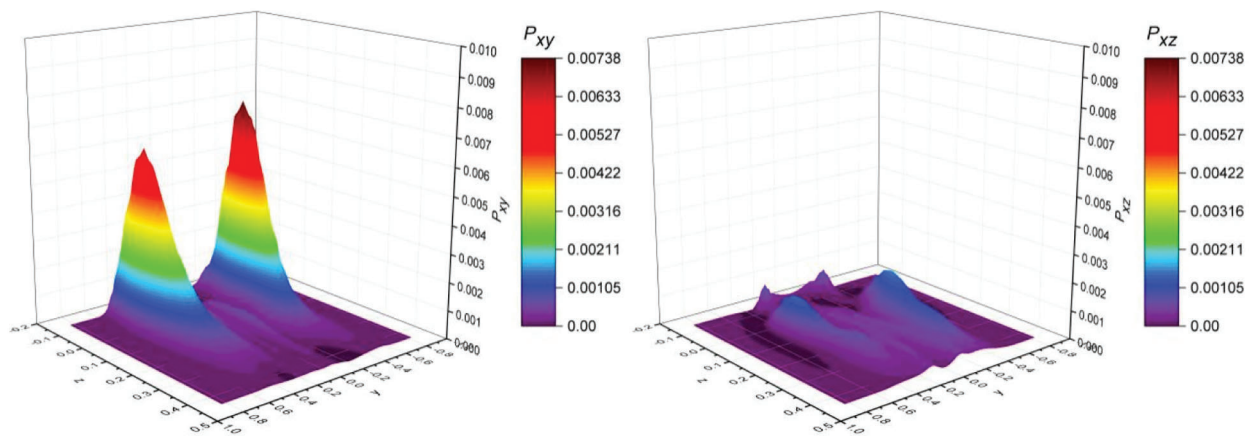

Figure 9: Comparison between the P_{xy} and P_{xz} distributions corresponding to the streamwise position, $x = 2H$ (the M4 case)

3.4 Discussions

Considering the characteristics of the y-z plane distributions of the TKE and TP at $x = 0$, H and $2H$, it is not difficult to find that the significant influences on the near wake of a high-speed train are exerted by the shear flows.

Due to the boundary layer separated and the low-pressure region formed, the flow around is forced to move towards the near wake and interacts with the flow from the underbody region, thus forming the strong

vortex pair. It is clear that, in the immediate vicinity of the tail, separated shear flows related to boundary layers are regarded as a significant mechanism in the local complex flow. According to the y-z distributions at $x = 0$ of the TKE and TP, the shear separated from the underbody region serves to make a great contribution to the local complex flow. The strong eddies can absorb energy of the mean flow rather quickly at the lower altitude thanks to the active interaction with the mean shear stress in the x-z plane during the formation and shedding of the wake vortices. Meanwhile, the separated shear flows, depending on the boundary layers on the side-wall surfaces of model, are of equal importance, but seem relatively low efficient to the turbulence production process. An explanation for this is that there are the much thicker boundary layers on both the side walls of the models, especially at the lower altitude close to the ground, so that the momentum thickness increased implies the decreased vorticity and strain rate of the shear layer, and eddies of larger scale have to stay in step temporally with the mean shear, resulting in the relative low rate of production of turbulent energy. Similarly, the increased streamwise length of train model surely leads to the thicker boundary layer, and thus with the momentum thickness increasing and vortex strength weakening, the mean-flow energy enters the turbulence mainly at the larger scale comparable to the integral length. So, compared with the M2 case, the TP (including P_{xy} and P_{xz}) very close to the tail are evidently low in the M4 case.

Therefore, an important fact can be revealed that the separated shear flows are governed by the boundary layers, thus playing dominant roles in turbulent wake around the tail and locally leading to the sensitivity of turbulent energy and its production to the strength of shear.

However, the significant influence of the strong shears has to be regretfully confined within very limited streamwise distance, and make few contributions for turbulent eddies away from the tail to extracting the mean-flow energy downstream. And the streamwise length effect becomes of little importance downstream, as indicated by the findings for the streamwise positions away from the tail ($x = H$ and $2H$). It is believed that both vorticity and deformation are important to define a 'vortex'. Undoubtedly, the dominant shears separated from the boundary layers play great roles in vorticity and deformation for the streamwise vortices, but in the meantime, tend to be of high dissipation.

When the vortices are formed and then propagated downstream along the streamwise direction, eddies away from the tail continue obtaining the mean-flow energy transferred to the turbulent wake at a low rate. Interestingly, this physical process is mainly due to the mean shear strain rate in the x-y plane.

It is shown in Fig. 10 that the streamwise vortex (a vortex core marked with the line and asterisk) moves downwards and outwards when progressing away from the tail, probably due to the mutual induction and interaction with the ground. The phenomenon resembles the so-called common-flow-down type of vortex pair in Pauley et al. [23] where it was suggested that the interaction between the vortices and the ground can lead to the diffusion of vorticity as a result of the distortion in the stress field, hence diminishing the vortex strength. The interaction with the ground is an important mechanism for the similar vortex structure in Corjon et al. [24]. Accordingly, vortical motion with the center of the vortex core gets closer to the ground (in Figs. 10b and 10c) and interacts with the non-slip ground, as a result, the flow mechanism can has an impact on the local velocity and stress filed, not only responsible for the decaying vortex strength but also beneficial to the x-y plane shear stress and thus the P_{xy} component of TP.

Unlike the shear deformation near the tail end, the vortical motion with lower vorticity is dissipated more slowly [25]. Hence, the interaction between the streamwise vortices and the ground can maintain the mean shear strain rate in the x-y plane for a longer distance along the streamwise direction. In addition, the mechanism obviously has nothing to do with the lengths of the train models, so there are similarities between the M2 and the M4 case concerning the local y-z plane distributions of the TP.
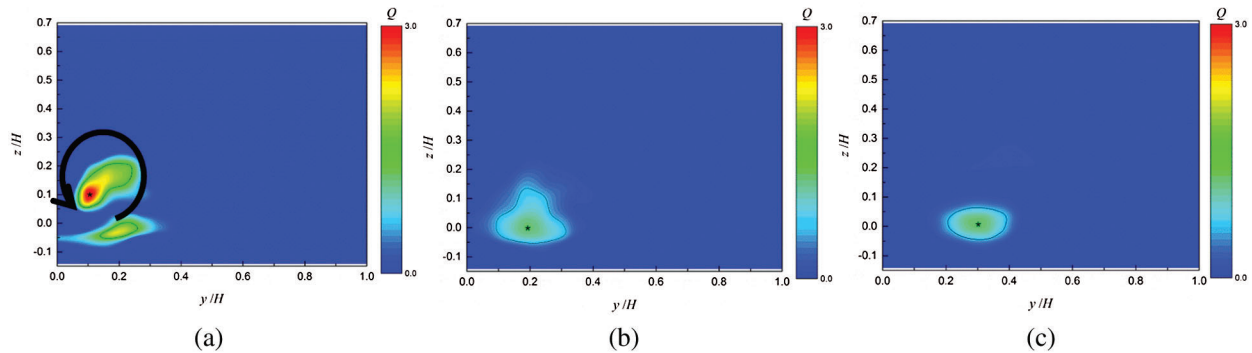
(a)   (b)   (c)

Figure 10: Time-averaged *y-z* contours of the *Q* at the varied streamwise positions, $x = 0.5H$, $2H$ and $4H$ (the M2 case). (a) $x = 0.5H$ (b) $x = 2H$ and (c) $x = 4H$

4 Conclusions

From the viewpoint of turbulent energy, an investigation has been made on the shear flows and related flow mechanisms in the near turbulent wake of high-speed trains.

According to the notable feature presented by the local *y-z* plane distributions of the TKE and TP, it is observed that, in the near wake region around the tail, the strong shears are governed by the boundary layers developed along the streamwise direction on the train surfaces, especially from the underbody region and both the side walls, and make remarkable contributions to the local turbulence. But the notable deformation during the formation of wake vortices leads to high dissipation of the shear strength.

For the downstream positions away from the tail, the larger eddies can still keep obtaining the mean-flow energy, although energy transfer seems not very efficient any more. The interaction between the streamwise vortices and the non-slip ground is thought of as a major mechanism to maintain the mean shear strain rate in the *x-y* plane, which, however, seems not benefit to the rapidly weakening P_{xz} related to the mean shear in the *x-z* plane. And weak vortices with vortical vorticity of low magnitude can let the flow mechanism play a relative stable role in the evolution of the turbulent wake structure for a long streamwise distance.

Conflicts of Interest: The authors declare that they have no conflicts of interest to report regarding the present study.

References

1. Liu, J., Yu, M., Chen, D., Yang, Z. (2020). A study on the reduction of the aerodynamic drag and noise generated by the roof air conditioner of high-speed trains. *Fluid Dynamics & Materials Processing, 16(1),* 21–30.

2. Yu, M., Pan, Z., Liu, J., Li, H. (2020). Operational safety assessment of a high-speed train exposed to the strong gust wind. *Fluid Dynamics & Materials Processing, 16(1),* 55–66.

3. Li, H., Yu, M., Zhang, Q., Wen, H. (2020). A numerical study of the aerodynamic characteristics of a high-speed train under the effect of crosswind and rain. *Fluid Dynamics & Materials Processing, 16(1),* 77–90.

4. Bell, J. R., Burton, D., Thompson, M. C., Sheridan, J., Herbst , A. (2015). Moving model analysis of the slipstream and wake of a high-speed train. *Journal of Wind Engineering and Industrial Aerodynamics, 136,* 127–137.

5. Bell, J. R., Burton, D., Thompson, M. C., Sheridan, J. (2016). Flow topology and unsteady features of the wake of a generic high-speed train. *Journal of Fluids & Structures, 61,* 168–183.

6. Bell, J. R., Burton, D., Thompson, M. C., Sheridan, J., Herbst, A. H. (2016). Dynamics of trailing vortices in the wake of a generic high-speed train. *Journal of Fluids & Structures, 65,* 238–256.

7. Morel, T. (1978). *The Effect of Base Slant on the Flow Pattern and Drag of Three-dimensional Bodies with Blunt Ends,* In: G. Sovran, T. Morel, W. T. Mason (eds.), *Aerodynamic Drag Mechanisms of Bluff Bodies and Road Vehicles*, Springer, Boston, MA. DOI 10.1007/978-1-4684-8434-2_8.

8. Yao, S. B., Guo, D. L., Yang, G. W., Li, M. G. (2012). Distribution of high-speed train aerodynamic drag. *Journal of the China Railway Society, 34(7),* 18–23.

9. Zhang, J., Guo, T., Sun, B. C., Zhou, S. Z., Zhao, W. Z. (2015). Research on characteristics of aerodynamic noise source for high-speed train. *Journal of the China Railway Society, 37(6),* 10–18.

10. Baker, C. J. (2010). The flow around high speed trains. *Journal of Wind Engineering and Industrial Aerodynamics, 98(6–7),* 277–298.

11. Baker, C. J., Dalley, S. J., Johnson, T., Quinn, A., Wright, N. G. (2001). The slipstream and wake of a high-speed train. *Proceedings of the Institution of Mechanical Engineers Part F: Journal of Rail & Rapid Transit, 215(2),* 83–99.

12. Baker, C. J., Quinn, A., Sima, M., Hoefener, L., Licciardello, R. (2014). Full-scale measurement and analysis of train slipstreams and wakes. Part 1: Ensemble averages. *Proceedings of the Institution of Mechanical Engineers Part F: Journal of Rail & Rapid Transit, 228(5),* 451–467.

13. Rowe, A., Fry, A. L. A., Motallebi, F. (2001). Influence of boundary-layer thickness on base pressure and vortex shedding frequency. *AIAA Journal, 39(4),* 754–756.

14. Muld, T. W., Efraimsson, G., Henningson, D. S. (2014). Wake characteristics of high-speed trains with different lengths. *Proceedings of the Institution of Mechanical Engineers Part F: Journal of Rail & Rapid Transit, 228(4),* 333–342.

15. Tennekes, H., Lumley, J. (1972). *A first course in turbulence*. MIT Press, Cambridge, MA.

16. Huang, S., Hemida, H., Yang, M. Z. (2016). Numerical calculation of the slipstream generated by a CRH2 high-speed train. *Proceedings of the Institution of Mechanical Engineers Part F: Journal of Rail & Rapid Transit, 230,* 103–116.

17. Muld, T. W., Efraimsson, G., Henningson, D. S. (2012). Flow structures around a high-speed train extracted using proper orthogonal decomposition and dynamic mode decomposition. *Computers & Fluids, 57(4),* 87–97.

18. Yao, S. B., Sun, Z. X., Guo, D. L., Chen, D. W., Yang, G. W. (2013). Numerical study on wake characteristics of high-speed trains. *Acta Mechanica Sinica, 29(6),* 811–822. DOI 10.1007/s10409-013-0077-3.

19. Shur, M. L., Spalart, P. R., Strelets, M. K., Travin, A. K. (2008). A hybrid RANS-LES approach with delayed-DES and wall-modelled LES capabilities. *International Journal of Heat and Fluid Flow, 29(6),* 1638–1649. DOI 10.1016/j.ijheatfluidflow.2008.07.001.

20. Hemida, H., Baker, C., Gao, G. (2014). The calculation of train slipstreams using large-eddy simulation. *Proceedings of the Institution of Mechanical Engineers, Part F: Journal of Rail & Rapid Transit, 228(1),* 25–36. DOI 10.1177/0954409712460982.

21. Bell, J. R., Burton, D., Thompson, M., Herbst, A., Sheridan, J. (2014). Wind tunnel analysis of the slipstream and wake of a high-speed train. *Journal of Wind Engineering and Industrial Aerodynamics, 134,* 122–138. DOI 10.1016/j.jweia.2014.09.004.

22. Jeong, J., Hussain, F. (1995). On the identification of a vortex. *Journal of Fluid Mechanics, 285(4),* 69–94. DOI 10.1017/S0022112095000462.

23. Pauley, W. R., Eaton, J. K. (1988). Experimental study of the development of longitudinal vortex pairs embedded in a turbulent boundary layer. *AIAA Journal, 26(7),* 816–823. DOI 10.2514/3.9974.

24. Corjon, A., Poinsot, T. (1997). Behavior of wake vortices near ground. *AIAA Journal, 35(5),* 849–855. DOI 10.2514/2.7457.

25. Liu, C. Q., Wang, Y. Q., Yang, Y., Duan, Z. W. (2016). New omega vortex identification method. *Science China Physics, Mechanics & Astronomy, 59(8),* 684711. DOI 10.1007/s11433-016-0022-6.